

Cite this: *Nanoscale*, 2018, **10**, 1680

Computational insight into the origin of unexpected contrast in chiral markers as revealed by STM[†]

Ana Sanz-Matías,^{ID *a} Oleksandr Ivasenko,^b Yuan Fang,^b Steven De Feyter,^{ID b} Kazukuni Tahara,^{c,d} Yoshito Tobe^{ID c,e} and Jeremy N. Harvey^{ID *a}

Internal substituents can serve the double purpose of generating stereogenic centers and (potentially) being identifiable with Scanning Tunneling Microscopy (STM) in 2D self-assembled molecular layers. We investigate computationally the origin of stark contrast variations in STM images of chirally substituted self-assembled organic films. STM images of alkyl derivatives with secondary –CH₃ and –OH groups have been simulated. Density functional theory calculations reveal bias-dependent contrast reversals in the substituent regions: a lack of local density of states in the relevant energy regime results in ‘dark spots’ in the simulated STM images, which turn bright upon increasing the bias voltage.

Received 4th October 2017,
Accepted 6th December 2017

DOI: 10.1039/c7nr07395j

rsc.li/nanoscale

1 Introduction

The investigation of chiral supramolecular architectures is key because of its relevance to material sciences. Molecular self-assembly at the liquid–solid interface has attracted increasing attention as a confined, lower-dimensionality medium in which to probe fundamental aspects of on-surface chirality as well as to bring insight in a variety of applications ranging from enantioselective heterogeneous catalysis to chiral separation.^{1–3}

Achiral as well as chiral molecules have the potential to form highly regular supramolecular networks on atomically flat substrates. In mono-component systems, achiral building blocks can form mirror image domains and hence exhibit local chirality. However, achieving global surface chirality requires chiral building blocks: enantiopure compounds that assemble into domains with identical handedness. In bi-component systems consisting of achiral molecules and a small

amount of a chiral modified dopant, the latter can dictate the formation of domains of specific handedness to the remaining achiral components, hence resulting in assemblies with global chirality. This is known as the ‘sergeants and soldiers’ effect.⁴ Typically chiral analogues of the otherwise achiral building blocks are obtained *via* substitution creating one or more chiral centers retaining most structural features of the original.⁵ Secondary methyl groups are often the substituent of choice due to their synthetic feasibility and ‘innocence’ (*i.e.*, they introduce little chemical variability other than generating a stereogenic center).

The characterization of such layers is primarily achieved using Scanning Tunneling Microscopy (STM) as a nanoscale probe. Provided the substrate is electrically conductive and atomically flat, STM allows imaging the molecular structure of the layer in great detail. Although STM images are often discussed and related to the nanostructures they represent in topographic terms, electronic effects play a key role. Identification and analysis of the images often rely on the careful measurement of packing distances, the observation of distinct submolecular features (*e.g.* substituents or strategically placed metal atoms) and the complementary theoretical support from atomistic simulations of the molecular adlayer.^{6,7} Functional groups which display unusual image contrast relative to the surrounding molecule moieties are considered STM markers and serve as ‘flags’, making it possible to identify and discriminate structures more accurately within individual molecules.⁸

Combining the functions of chirality and STM marker within the same functional group is thus convenient not only for chirality induction, but also for identification of the chiral

^aQuantum Chemistry and Physical Chemistry, Department of Chemistry, KU Leuven, BE-3001 Leuven, Belgium. E-mail: jeremy.harvey@kuleuven.be, ana.sanzmatias@kuleuven.be

^bMolecular Imaging and Photonics Section, Department of Chemistry, KU Leuven, BE-3001 Heverlee, Belgium

^cDivision of Frontier Materials Science, Graduate School of Engineering Science, Osaka University, Toyonaka, Osaka 560-8531, Japan

^dDepartment of Applied Chemistry, School of Science and Technology, Meiji University, Kawasaki, Kanagawa 214-8571, Japan

^eThe Institute of Scientific and Industrial Research, Osaka University, Ibaraki, Osaka 567-0047, Japan

[†] Electronic supplementary information (ESI) available. See DOI: 10.1039/C7NR07395J

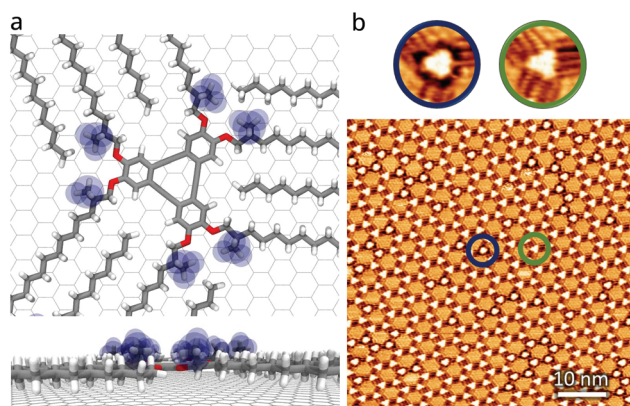


Fig. 1 Methylated DBA derivatives present 'dark contours' in STM images. (a) Top view and side view of an atomic model of cDBA-OC12(S)-OC13(R) embedded on a molecular layer on graphene. The methyl substituents point away from the surface. Their van der Waals surface, which results from assuming each atom to be a hard sphere of $r = r_{vdW}$ is shown in blue. (b) Experimental STM constant-current image of a mixture of cDBA-OC12(S)-OC13(R)/DBA-C12 ($V_{bias} = -0.2$ V, $I_{set} = 0.21$ nA). cDBA-OC12(S)-OC13(R) molecules have 'dark contours' (detail in blue) while DBA-C12 molecules do not (detail in green) ($V_{bias} = -0.2$ V, $I_{set} = 0.21$ nA).

dopant in bi (or multi)-component systems. This facilitates physico-chemical studies of various kinetic and thermodynamic interfacial phenomena. An example of chiral substituent/STM marker unification is the bi-component system formed by alkoxylated dehydrobenzo[12]annulene derivatives (DBAs) and their chiral methylated counterparts (cDBAs).⁹ This system has been thoroughly investigated in, among others, 'sergeants and soldiers' experiments.¹⁰ In the STM images of DBA/cDBA films formed on highly ordered pyrolytic graphite (HOPG), the chiral building blocks are characterized by the so-called 'dark contours'¹¹ that appear in the regions where the methyl chiral substituents are located (Fig. 1). Further details on the experimental STM images can be found on the ESI (section S1†). Other systems in which the methyl chiral substituent/marker has been imaged are long alkanes¹² ‡ and a terephthalic acid derivative,¹⁴ both on HOPG. These are, to our knowledge, the only cases in which the appearance of methyl markers in STM images has been recorded.

Nevertheless, stark contrast variations have been reported: internal methyl markers have been associated to bright regions in the STM images of long alkanes,¹² to 'dark contours' in the cDBAs images,¹¹ and to 'streaky features' and 'lack of resolution' in the case of the terephthalic acid derivative images.^{14,15} Since these are constant-current images, brighter implies the tip retracting from the surface. This means that for the same chemical functional group, the position of the tip varies greatly in order to sustain a constant tun-

‡ Interestingly, methylated long alkanes are widely present in insect outer cuticles and are involved in insect chemical communication systems.¹³

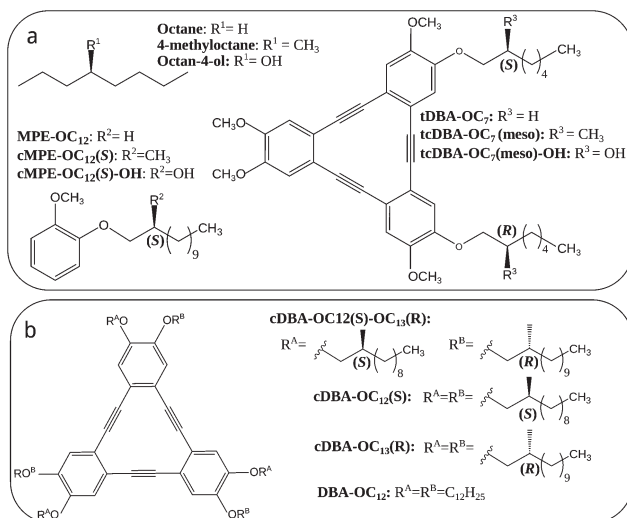
neling current. From the topographical point of view, one would expect the protruding marker groups to appear as bright features, *i.e.* lying high above the mean level of the film, in contradiction with the reported 'dark contours'. In assemblies on metallic surfaces, physical protrusions may not always result in brighter features.^{16,17} However, such stark contrast variations are less common in images of organic films on graphite.

We aim to investigate the origin of these contrast variations (bright, non-visible and dark) through a computational approach involving electronic structure calculations as well as STM image simulation. Understanding the origin of such sub-molecular contrast may assist improved design of other STM markers. Most *ab initio* studies of STM images use a variety of density functional theory (DFT) together with periodic models in two dimensions of the substrate and the film. We used this procedure together with a standard generalized gradient approximation (GGA) DFT functional, PBE, in some parts of this work. As discussed below, though, this methodology leads to some significant inconsistencies between the predicted images and experiments, that appeared to be due to the theoretical ansatz. Indeed, the well-known self-interaction error (SIE) can affect the degree of orbital localization which in turn leads to errors in the spatial distribution of STM image features.¹⁸ This led us to carry out additional calculations using hybrid DFT functionals, which are approximately SIE-free.

Here we report a systematic investigation of the effect that secondary methyl and hydroxyl substituents have on the STM appearance of molecular adsorbates. Our calculations involve a small alkane and a DBA derivative marked with methyl substituents, inspired by the aforementioned experimental results. To assess the electronic effects of the DBA core group, it was also useful to consider a model of intermediate size, 2-methoxyphenyl 2-methyldecyl ether (cMPME-OC₁₂(S)). Available experimental data for hydroxylated alkanes^{12,19} motivated us to also investigate the appearance of hydroxy markers. We report these calculations also as they have the benefit of providing a broader basis of insight into the appearance of these markers. The non-methylated and non-hydroxylated compounds were also studied for reference purposes, leading in summary to the set of species shown in Scheme 1.

2 Computational details

The structures used in calculations of STM images were obtained based on geometry optimization using molecular mechanics (MM). For the MM calculations, periodic boundary conditions were applied with supercells containing the adsorbate molecule or molecules as well as a two-layer graphite substrate. The atomic coordinates of the adsorbate molecules in these supercells were optimized (RMS gradient threshold: 0.01 kcal mol⁻¹ Å⁻¹) using the Tinker package.²⁰ The OPLS-AA²¹ force-field, which reproduces adequately the interactions present in these type of systems (see section S8 in the



Scheme 1 Some of the molecular species investigated computationally (a) have also been studied experimentally here (b) and elsewhere.^{9–12,19}

ESI[†]), was used for all atoms. Appropriate OPLS-AA atom types were assigned to all species studied here without modification, except for the case of the graphene substrate. Here, an aromatic carbon atom type was used, modified to have a zero charge. The substrate atoms were kept fixed throughout the optimization process. In all cases, the size of the supercell in the direction orthogonal to the substrate was of >32 Å, which is sufficient to prevent interactions between the periodic images in this dimension. The size of the supercell in the two other dimensions was chosen based on the adsorbate in such a way as to prevent interactions of the adsorbates with themselves.

STM images were computed based on two different DFT approaches. The first approach used the SIESTA²² code together with periodic boundary conditions and the Perdew–Burke–Ernzerhof²³ GGA exchange–correlation functional. In SIESTA, core electrons are replaced by norm-conserving Troullier–Martins-type pseudopotentials.²⁴ A double- ζ plus polarization basis set was used for valence electrons. The pseudo-atomic orbital (PAO) energy shift, which defines the orbital confinement radii was set to 0.01 Ry so as to minimize the total energy. The energy cutoff of the real space integration mesh was 220 Ry. To ensure the convergence, the reciprocal space was sampled using a $3 \times 3 \times 1$ Monkhorst–Pack k -point grid. The MM structures from Tinker were used directly in these calculations after adjusting the shape of the supercell, and in some cases deleting the second graphene layer. The size of the supercell was again chosen to be large (>27 Å) in the vertical direction, and sufficiently large to prevent spurious contacts in the other directions: 12 × 12 for the octane and MPE derivatives, and 16 × 16 in the case of the DBA derivatives.

The second set of electronic structure calculations used the Gaussian 09 program package²⁵ together with a hybrid functional comprising full (100%) Hartree–Fock treatment of

exchange, and the PBE²³ correlation (see ESI, section S2†). Below, we refer to this as the 100PBE functional. All atoms were treated using the 6-311G* basis set. For these calculations a cluster, non-periodic, model was used, generated by modification of the MM-optimized supercell geometries. The C–C bonds that were cut to generate the polycyclic hydrocarbon model of the graphene sheet were saturated with hydrogen atoms, and the cut was carefully chosen to yield an even number of π electrons. The graphene ‘flake’ thus generated was typically slightly smaller than the supercell but still large enough that the regions of interest in the adsorbate were well separated from the flake edge.

Then, STM images based on both the SIESTA and Gaussian 09 Kohn–Sham orbitals were simulated with the Tersoff–Hamann approximation.²⁶ The local density of states (LDOS), proportional to the tunneling current, is a function of position and energy. Integration within the energy range defined by $[E_F - eV_{\text{bias}}, E_F]$, where E_F is the Fermi energy and V_{bias} the bias voltage, was directly performed in SIESTA. For the cluster calculations, we instead had to obtain the integrated LDOS by summing the densities associated with the highest energy orbitals within the aforementioned energy range. E_F was here taken to be the energy of the Kohn–Sham HOMO. The code used to perform this summation for the Gaussian calculations is provided in the ESI (section S3†). Constant-current images were then simulated by obtaining isosurfaces of the integrated LDOS using ‘plstm’, an utility included in the SIESTA package. Fine tuning of the simulation parameters is discussed later on. To facilitate the comparison between images, we used the same colour-scale in all of them: 1–8 Å, where the 0 Å indicates the position of the graphene carbon nuclei.

3 Results and discussion

The motivation of this study was to provide a computational modelling insight into the appearance of chiral methyl and hydroxy substituents in STM images of organic films.

The first two sections cover general descriptive aspects regarding the image simulation parameters and system geometries. First, we describe the general procedure we followed to calculate the image simulation parameters which enable a correct mapping between experimental and simulated images (section 3.1). We then consider how structural features, specially around the markers, may affect the images (section 3.2).

The following section (section 3.3) describes the results obtained for the methylated molecules in Scheme 1. We found it illustrative to start from the smallest system, 4-methyloctane, and examine some surface effects in the calculated images, as well as the relation between image topography, physical topography and electronic structure, especially around the marker. We then discuss the changes in electronic structure and density brought about by the small aromatic ring in MPE-OC₁₂, which anticipates those taking place in the larger tDBA-OC₇ and its derivatives. Two aspects are key: the effect of

self-interaction error in the electron density shape (which prompted a change in the methodology), and the decay of charge density in the vertical direction to the surface. Lastly, we report the effect of marker orientation in tcDBA-OC₇(*meso*) calculated images as compared to the reference system.

In section 3.4, we summarize the results for the hydroxy marked compounds by highlighting the main differences with respect to the methyl markers. Finally, in section 3.5 we discuss a few general questions that arise in view of the results, such as the role of bias voltage and electronic structure particularities in image contrast and, more specifically, in the origin of the cDBA ‘dark contours’ observed experimentally.

3.1 Image simulation parameters and mapping to experiment

Comparing simulated STM images to experimental ones requires some care, so as to obtain a meaningful mapping of the computational parameters to the experimental settings (bias voltage, V_{bias} , and tunnelling current, I_t). We have found it helpful to establish from first principles the computational settings needed to reproduce a given experimental image. We have done this within the Tersoff–Hamann approximation, but also with awareness of the shortcomings of this model. In most cases, we focus on simulating images acquired with negative sample bias, *i.e.* in which the tunneling electron flow is from the substrate to the tip, and our description below reflects this focus. In some cases, though, we will also discuss positive bias images, and the changes to the framework described below will be mentioned as appropriate.

In the Tersoff–Hamann approximation, the tunnelling current is proportional to the integrated local density of states (iLDOS) and a prefactor C :

$$I_t = C \int_{E_F}^{E_F + eV} \rho(\mathbf{r}, E) dE \quad (1)$$

This can be re-written in terms of a sum over Kohn–Sham orbitals, also referred to as tunneling states:

$$I_t = C \sum_{i=1}^n |\Psi_i(\mathbf{r}_0)|^2 \quad (2)$$

where $\Psi_i(\mathbf{r}_0)$ is the sample state with energy ϵ_i evaluated at the point situated at the centre of curvature of the STM tip, \mathbf{r}_0 . The number of tunnelling states included in the summation, n , is chosen based on the condition that $\epsilon_n - E_F \leq eV$.

Hence, the bias voltage used in experiments (V_{bias}) can be directly related to state energies and defines, within the Tersoff–Hamann approximation, the energetic range of the tunnelling states that contribute to the image, influencing its size and shape.²⁷ The energy, shape and symmetry of the states of the substrate + adsorbate supersystem from which the electrons tunnel to the tip depend strongly on the details of the substrate and adsorbate electronic states and their coupling. While the strong coupling in metallic substrates can heavily alter the molecular electronic structure,²⁸ with insulating substrates, the coupling is weaker and the images more

directly reflect the native charge density distribution of the adsorbates.²⁹ In the present case, with the weakly-interacting, semi-metallic graphene substrate, the situation is closer to the second of these two limits (see ESI, section S4†). For some of the adsorbates we study here, the highest energy orbitals of the molecule lie close to the Fermi level of the whole system. However, for other adsorbates, especially with the relatively low bias voltages that are experimentally relevant, the tunnelling states are mostly associated with HOPG bands, with only a small admixture of the adsorbate orbitals. In this framework, in order to define the energy scale used to generate the integrated LDOS, it is absolutely essential to include a section of the substrate in the calculations.

We will compare our calculated images against experimental images acquired specifically for this purpose, such as those in Fig. 1(b) and 7, and STM images in the literature, from ref. 9–12 and 19. The bias voltage at which these images were acquired spans from −0.4 V (for chiral DBA films^{9–11}) to +1.4 V (for long alkane films^{12,19}). Although the difference in these values of bias voltage may seem relatively low, the marker appears as a depression in the former images and as a protrusion in the latter, as mentioned in the introduction.

This significant difference led us to choose representative images of both extreme situations from arrays of images of each adsorbate in which a similar range of bias voltages was sampled. The result is two bias voltage regimes which we label as ‘small’ and ‘large’. Since the bias voltage is explicitly accounted for in the SIESTA calculations, these regimes have defined numerical values in the case of the SIESTA calculations and correspond with bias voltage values below |0.5| V, and above |1.0| V, much as in experiment.

In the Gaussian calculations, however, our procedure only allows approximate specification of the bias voltage. We have again aimed for the two regimes just mentioned.

Along with the bias voltage, an estimate of the prefactor C is necessary to evaluate I_t^{calc} . C depends on the characteristics of the tip and sample:

$$C = 32\pi^3 \hbar^{-1} e^2 V \phi^2 D_t(E_F) R^2 \kappa^{-4} e^{(2\kappa R)}$$

where ϕ is the work function of the substrate–adsorbate system, D_t is the density of states at E_F per unit volume of the probe tip, R is the radius of curvature of the tip, and $\kappa = \hbar^{-1} \sqrt{2m\phi}$ is the minimum inverse decay length in vacuum of the wavefunction of the substrate–adsorbate system.

To estimate C , we use a bias voltage of 2 V, a workfunction of 4.5 eV,³⁰ D_t of $10^{38} \text{ eV}^{-1} \text{ m}^{-3}$ (typical for Si) and $R = 1.6 \text{ \AA}$.³¹ In the constant-current imaging mode, I_t^{exp} is usually in the range of picoamperes (pA) to nanoamperes (nA). With the value of C used here, an isocurrent in the nA regime is obtained with an iLDOS value of the order of $10^{-6} \text{ e bohr}^{-3}$. To account for the errors in our estimation and the experimental isocurrent window of almost three orders of magnitude, the constant-current simulated images examined in this study were calculated at iLDOS values of 10^{-7} to $10^{-5} \text{ e bohr}^{-3}$.

3.2 Geometries

The geometrical structures used in the first-principles calculation of STM images were derived from molecular-mechanics based geometry optimizations. In all of them, alkyl chains adopt extended (all-anti) conformations oriented along one of the main symmetry axes of graphene, in agreement with the literature.^{32,33} The zig-zag of the carbon chain is parallel to the plane of graphene as shown in Fig. 2(d). The adsorbate–substrate distance, measured from the carbon nuclei in the graphene to the carbon nuclei in the molecules, is roughly 3.6 Å within the region of the alkyl chains. The aromatic fragments in tDBA-OC₇ and MPE-OC₁₂ derivatives lie flat, and closer to the surface by ~0.2 Å. In the hydroxylated derivatives of tDBA-OC₇ and MPE-OC₁₂ there is an intramolecular hydrogen bond between the ether oxygen and the hydrogen from the hydroxy marker in C2, two carbon atoms away. The oxygen–hydrogen distance is approximately 2.1 Å.

The presence of ‘bulky’ markers in the stereogenic center(s) of the molecules introduces two possible orientations with respect to the surface: “up”, with the –OH or –CH₃ substituents pointing towards the liquid phase, or “down”, with the group pointing towards the surface. According to the MM calculations, adsorption in the “up” orientation is preferred due to steric factors, specially in the methylated derivatives. The differences in total energy of the “up” and “down” orientations reach –1.7, –3.0 and –6.7 kcal mol^{–1} for 4-methyloctane, cMPE-OC₁₂(S) and tcDBA-OC₇(meso), respectively. For the hydroxylated counterparts, the differences in total energy also suggest a preference for the “up” orientation. However, in this case the energy differences are smaller (section S5†), and for octan-4-ol and tCDBA-OC₇(OH) a preference cannot be assumed. It is worthy of note that in the case of chiral DBA molecules, these energetic differences between orientations are a decisive factor in chiral monolayer formation.³⁴

The three chiral DBA molecules that have been reported to display ‘dark contours’ are named cDBA-OC12(S)-OC13(R), cDBA-OC13(R) and cDBA-OC12(S) (Scheme 1b).^{9–11} Each molecule has six stereogenic centers, with one substituent at each C2 position of the alkyl chains. The chirality of each marker is

either *R* or *S*. The pattern of stereochemistry is repeated around the cDBA cores following the threefold symmetry. Depending on the relative orientation of the markers within each molecule, chiral DBAs can be classified in two categories. All the markers point to the same side of the molecular core in cDBA-OC12(S)-OC13(R) (Fig. 1a). When it self-assembles on the surface, the “up” orientation will clearly be favoured, for the reasons explained above. In contrast, the markers in cDBA-OC13(R) and cDBA-OC12(S) have alternating orientations. On-surface, the presence of an “up” marker forces the neighbouring ones to be in the “down” orientation. However, variations in ‘dark contour’ shape and size among the three molecules are very difficult to detect due to limitations in STM image resolution. We considered that investigating only the (*S*, *R*) isomer (in both orientations) was sufficient for the purpose of this study, since our interest lies in the locality of each “up” or “down” group.

In addition, the influence of solvation and packing on the orientation of the adsorbed molecules with respect to the substrate should be briefly considered. These factors can in some cases play a key role in the self-assembly process. We note, however, that solvation and packing do not intervene directly in the tunneling process that determines bias-voltage STM imaging contrast. Hence, we have mostly not accounted for solvation or packing in our present calculations, as we feel that our models can reproduce the key structural features without needing to do so. Non-polar solvents such as 1-phenyloctane are used for assembly of the type of films studied here.^{11,12} The preference for “up” orientation of the chiral markers is highly unlikely to be modified by differential solvation effects with weakly interacting solvents such as phenyloctane. Ultimately, while calculations (here and in ref. 34) suggest that a larger stability is achieved in the structures where bulky markers point away from the surface, there is no conclusive experimental evidence of this, specially for the hydroxylated compounds. Nonetheless, experimental observations support that, in long alkane and chiral DBA layers, most methyl markers may be in the “up” orientation: in experimental STM images at large bias voltage of secondary long alkanes, bright regions can be clearly associated with the methyl markers.

With regards to packing, we included some extra alkyl chains only in the tDBA-OC₇ based geometries. The aim was to mimic the environment of the marker and ease the comparison with the experimental images.

3.3 Simulated images of methylated molecules

3.3.1 Calculated images of 4-methyloctane. Now we turn to the simulated images, and first consider the simplest adsorbates, octane and its methylated derivative, 4-methyloctane. Images of both adsorbates at small and large bias voltages are shown in Fig. 2, together with a van der Waals sphere atomic model of the geometry used for the 4-methyloctane adsorbate. The images in Fig. 2 were calculated with SIESTA, using the PBE functional and a periodic layer of graphene as substrate. Images calculated with bias voltages of –0.6 V and –2.0 V were chosen as particularly representative of the small and large

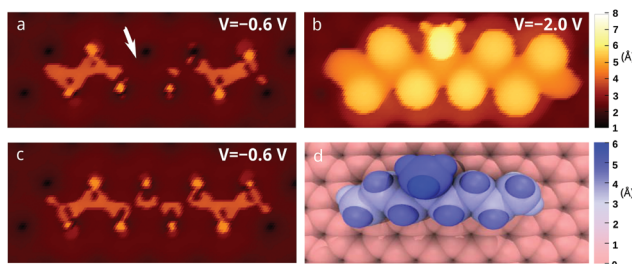


Fig. 2 Constant-current simulated images ($iLDOS = 10^{-6}$ e bohr $^{-3}$) of 4-methyloctane on graphene at small (a) and large (b) negative bias voltage, and of octane on graphene at small negative bias voltage (c). Space-filling geometry of 4-methyloctane on graphene coloured according to the z-coordinate of atom nuclei (d). The colour scales indicate height in angstroms. The arrow in (a) marks the ‘dark spot’.

bias voltage regimes (for a larger series of test calculations see section S6.1–S6.3†).

Calculated images of octane and 4-methyloctane adsorbates share several characteristics, although the methyl marker features introduce a differentiating element. In all images, two distinct groups of features can be identified: a darker region, corresponding to the bare graphene, and a brighter one, corresponding to the molecule. A series of bright spots arranged in a zig-zag fashion appear at about 3–4 Å above the apparent height of the graphene substrate. This zig-zag arrangement, which has been frequently observed in experimental images of alkanes, corresponds to the topmost hydrogen atoms and is associated to the carbon backbone of the molecule lying parallel to the surface.³² Upon an increase in the bias voltage, octane images remain largely unchanged, except for a steady rise in the apparent height of the molecular features. In 4-methyloctane images, however, the region corresponding to the methyl marker varies greatly in appearance upon changing bias voltage. Despite being the topmost part of the adsorbate–substrate system, at small bias voltage the image height in the methyl region is similar to that of bare graphene areas, *i.e.* the apparent ‘height’ is even lower than that of the corresponding hydrogen in the octane simulated image (Fig. 2a and c) or than the nuclei of the molecule. We will refer to this particular feature as the ‘dark spot’ (see section S6.5† for a side view). The image at large bias voltage (Fig. 2b) is in very good agreement with experimental observations, where the marker appears quite bright in comparison with the rest of the alkyl chain. Before discussing in detail this abrupt change, let us now examine how variations concerning the graphene substrate affect our calculated images.

3.3.1.1 Effect of substrate thickness and position. Incorporating the substrate in the calculations is key to obtain meaningful results, as mentioned before. For long alkanes, including only one layer of graphene to represent the HOPG substrate has been deemed insufficient to reproduce nuances in the relative contrast of hydrogen atoms.³³ Other authors have argued that grosser features such as the appearance of hydroxy markers at chain ends can be well captured using a single layer.³² In our case, test SIESTA calculations in which we have compared images obtained with different numbers of layers of substrate (section S6.2†) indicate that one layer is enough to reproduce the marker effects and variations thereof that are of interest here. Commensurability may also affect image contrast for pure alkane overlayers.³³ Nevertheless, for long alkanes and chiral DBA derivatives, STM marker regions show qualitatively invariable contrast within images regardless of packing and commensurability (as in Fig. 1 and 7), so we do not think that this is a major issue here.

3.3.1.2 Calculated image height. Fig. 2 focuses on qualitative features of the calculated STM images. It is interesting to compare, quantitatively, the height of the iLDOS isosurface to experimental tip heights in octane and 4-methyloctane images. Although experiment only provides information on relative heights, we find it convenient to introduce an absolute scale, expressed with reference to the vertical position of the

nuclei of the graphene substrate. In images simulated at small bias voltage (Fig. 2a and c), the iLDOS height ranges from 1.9 to 3.2 Å above different parts of the bare graphene surface, rises to 4.9 Å above the methylene portions of octane or 4-methyloctane and drops back to 3.2 Å above the methyl marker in 4-methyloctane (*i.e.*, the ‘dark spot’). For large bias voltage (Fig. 2b), the bare graphene features rise only slightly (of the order of 0.1 Å), whereas the methylene region LDOS height increases to 5.6 Å. The biggest change occurs above the methyl marker, where the LDOS isosurface rises to 6.4 Å, 3.2 Å higher than at low bias voltage. A summary can be found in Fig. 3. The orbital effects that account for these changes will be discussed below. Concerning the relative height between the methyl marker and the methylene regions, the closest experimental reference comes from the STM experiments in ref. 12, showing a difference of 0.74 ± 0.05 Å. These images were obtained at large positive bias voltage (+1.35 V, 200 pA). The calculated difference in iLDOS isosurfaces is 0.8 Å, in very good agreement with this experimental value. Imaging parameters closer to experiment ($V_{bias} = +1.35$ V, integrated LDOS 5×10^{-7} e bohr⁻³) yield an identical difference (0.8 Å). Comparison between experiment and computation at low bias voltage is not possible, because to our knowledge, ‘dark contours’ have never been observed for a simple methylated alkane. We suggest two reasons for the fact that such experiments have not been reported. Firstly, alkanes are difficult to image on HOPG at small bias voltages, with most published images using higher voltages, usually starting from absolute bias voltage values of 0.7 V and up to 2 V. Secondly, to our knowledge no STM studies have been published on mixtures of marked chiral and achiral alkanes, for which visualizing the marker – hence low bias imaging – would be of primary interest.

3.3.1.3 Dark spot, topography and electronic structure. The large difference in iLDOS isosurface height above the methylene and methyl marker regions is naturally in contrast with the respective heights of these groups in terms of their topo-

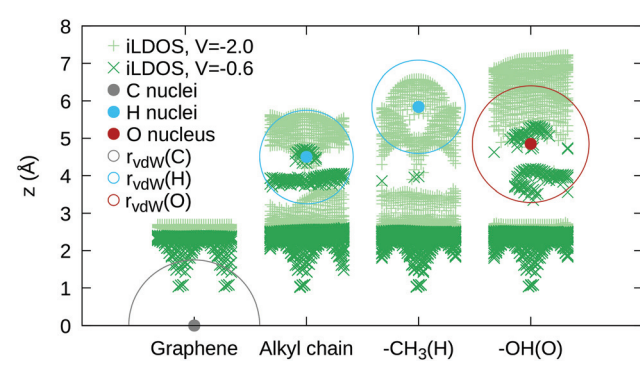


Fig. 3 Comparison of calculated image height, atomic nuclei height and van der Waals surface for octane with methyl and hydroxyl markers. Image heights at bias voltages $V = -0.6$ and $V = -2.0$ ($iLDOS = 10^{-6}$ e bohr⁻³) are shown in green. These points correspond to vertical (z) cuts of 2×2 Å² areas on the graphene, alkyl chain and methyl or hydroxyl marker on the calculated images of 4-methyloctane and octan-4-ol.

graphy, that is, their van der Waals (vdW) surfaces. Taking the van der Waals radius of carbon and hydrogen atoms to be 1.75 and 1.25 Å (as in the OPLS-AA force field), the vdW surfaces of the graphene flake, the topmost backbone hydrogens, and the topmost hydrogen of the methyl marker in 4-methyloctane lie at an average height of 1.75, 5.9 and 7.0 Å, respectively. That is, both low and high bias iLDOS isosurfaces lie above the vdW surface at some points of the adsorbate–substrate system, and well below the vdW surface in others (Fig. 3). For the bare graphene, image height is between 0.2 and 1.6 Å above the vdW surface, depending on the specific point and bias voltage. However, for the methylene regions of the molecule, the iLDOS isosurface lies below the vdW surface by close to 1 Å and 0.3 Å, at low and high bias voltage, respectively. Furthermore, in the methyl marker region, these distances amount to 3.8 and 0.6 Å.

From an electronic structure perspective, this inversion between image height and vdW surface in the region of the molecule can be explained looking at the spatial distribution of the electronic density in the tunneling states. The states that lie within the energy range used to calculate the images, even at large bias voltages, are mainly graphene-centered. These states nevertheless have density contributions in the region of the adsorbate due to the presence of orthogonalization tails³³ arising from weak mixing of adsorbate states with the graphene bands. The extent of this mixing is greater for higher-energy adsorbate orbitals, and also increases when there is greater spatial overlap with the graphene states. At larger bias voltage, the extent of mixed tunneling states also increases, hence the iLDOS in the adsorbate region is larger, leading to a higher predicted image height. The calculated image height in the region of the methyl marker is spectacularly lower than the van der Waals surface, with a difference of up to 3.8 Å. This is apparent in qualitative terms in Fig. 2a, where the whole region of the methyl group is near-invisible. One reason for this is that the HOMO of 4-methyloctane has almost no amplitude in the methyl region (see section S7† for orbital images; this is due to σ-hyperconjugation effects).³⁵ Another important factor is that the overlap with graphene states is much smaller due to the greater distance from the surface.

3.3.2 Calculated images of cMPE-OC₁₂(S). Let us now consider the methylated derivative of MPE-OC₁₂, cMPE-OC₁₂(S). An important difference with respect to the alkanes examined in the previous section is that the presence of a 2-methoxyphenyl ether functional group introduces occupied molecular orbitals of the adsorbate that are closer in energy to the Fermi level of the graphene substrate. These orbitals contribute significantly not only to the LDOS in the region above the aromatic group, but also impact the LDOS in the region of the chiral marker due to delocalization of electronic density. According to our periodic PBE calculations, the highest electronic state localized in the molecule is 0.7 eV below the Fermi level of the whole system. For octane, this difference was approximately 2.8 eV (Fig. S1†). With regard to the simulated images, one major consequence is that the aromatic fragment of the molecule is visible at smaller bias voltages and appears brighter than the alkane fragments.

3.3.2.1 Effects of self-interaction error. Focusing on the region of the methyl marker, there was a significant difference in the behaviour of the PBE calculated images compared to the 4-methyloctane case: at all bias voltages at which the alkyl chain was visible, including the ‘low bias’ case of $V_{\text{bias}} = -0.5$ V, the methyl marker appeared brighter, thus higher, than the remainder of the alkyl chain. Experimentally, in DBA derivatives, methyl markers appear dark at low bias voltages, inconsistent with this result. Test calculations with the methyl marker placed at a greater distance along the alkyl chain (see S6.6†) exhibit a return to the results obtained with 4-methyloctane. We also noted that in the images, the iLDOS associated with the methyl group appears to merge with that associated with the high energy electron density of aromatic ring. Electron density calculated with GGA DFT functionals such as PBE is known to be over-delocalized in some cases due to electron self-interaction errors (SIE),³⁶ as further discussed in the General discussion section. For all these reasons, we considered that the appearance of the calculated images might be an artefact of the PBE functional. Within SIESTA, it is not possible to carry out calculations that would be SIE-free. Accordingly, we performed calculations using the molecular quantum chemistry code Gaussian, a finite substrate–adsorbate model structure, and the approximately SIE-free 100PBE functional, in which the exchange part of the functional is entirely described by ‘exact’ Hartree–Fock exchange. As we expected, at this level of theory, the ‘density leaking’ from the aromatic group that causes the methyl marker to appear bright at all bias voltages is very significantly diminished, leading to the reappearance of a ‘dark spot’ at some bias voltages (Fig. 4). We note that calculated images of octane and 4-methyloctane using 100PBE and a non-periodic flake of graphene (see S6.1–S6.3†) are substantially similar to the ones shown in Fig. 2, which were calculated using PBE and a periodic graphene surface.

Graphene truncation to form a flake, as used in our 100PBE calculations, affects the band structure and orbital energies of the graphene substrate. In turn, this has consequences for the treatment of the bias voltage, which therefore differs slightly in the periodic and cluster calculations, even leaving aside the changes in functional (PBE vs. 100PBE) and basis set (DZP vs. 6-311G*). In our periodic calculations, the overall band structure of the graphene/graphite substrate agrees well with previously reported results (section S4†). Also, it is easy in this case to assign E_F , as it simply corresponds to the highest energy of the top filled band, that is at the K point in the Brillouin zone. In the cluster calculations, there are no bands as such, although the large size of the flake used does mean that some features of the band structure are effectively present. The HOMO will lie close in energy to where the top of the ‘band’ would be, but its energy is not guaranteed to correspond exactly to E_F . In our image calculations, we do assign E_F as being the HOMO eigenvalue, but this introduces a first uncertainty in our treatment of the bias voltage. Furthermore, the pattern of orbital eigenvalues below the HOMO in the flake calculations does not reflect the underlying symmetry of the graphene. For example, the highest band of graphene is

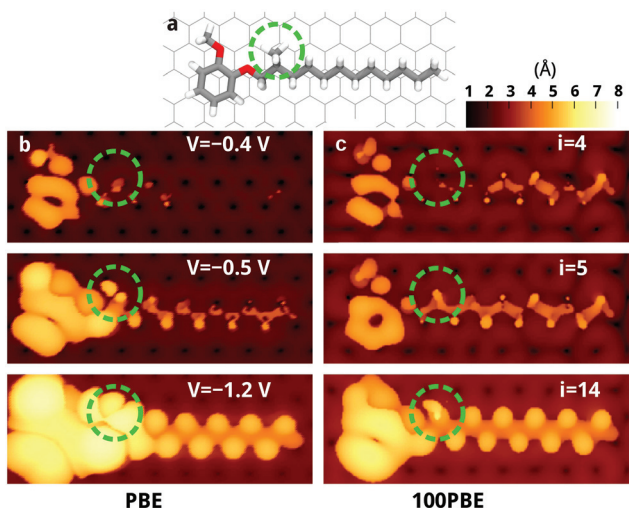


Fig. 4 Self-interaction error affects marker image contrast. (a) Atomic model of cMPE-OC₁₂(S) on graphene. Constant-current simulated images of cMPE-OC₁₂(S) on periodic graphene using PBE functional (b) and on a graphene flake using 100PBE functional (c), at different bias voltages (indicated by V , bias voltage, or i , the number of integrated orbitals) and an $iLDOS = 10^{-6}$ e bohr⁻³. The methyl marker region is signaled by a green circumference. The colour scale indicates height in angstroms.

degenerate in periodic calculations but not in the flake calculations. Picking the number of orbitals included in eqn (2) purely based on an energy interval with respect to the HOMO was observed to lead to artefacts in some cases. Instead, images were generated for ‘small’ and ‘large’ bias voltages based on summation over a definite number of orbitals ($i = 4$ and $i = 14$ respectively), with the number chosen to reproduce the main features of the images obtained from SIESTA – specifically the graphene features. The implied energy gaps do not exactly match those used in SIESTA, for the reasons just discussed. For the cMPE-OC₁₂(S) monolayer, for example, HOMO–3 lies 0.87 eV below the HOMO, and HOMO–14 lies 3.31 eV below.

3.3.2.2 Dark spot, image contrast and LDOS decay in space. So far, we have discussed in detail the main aspects of our simulated STM images such as substrate effects, bias voltage or image height. Simulated images depend on how well the decay of the wave functions in space is modelled, especially at small biases. Electron density – and hence tunnelling current – decays exponentially away from the sample, and the STM technique is very sensitive to this decay. Hence, we found it interesting to visualize the image height (z) as a function of the $iLDOS$ at small and large bias voltage (Fig. 5a). This type of plot provides insight into the decay of local charge density in space above a particular point in the plane defined by the adsorbate–substrate system, and at a specific bias voltage. We chose four representative points to establish a comparison between the main regions of interest within the cMPE-OC₁₂(S)–graphene system: one in an adsorbate-free region of the graphene surface, one directly above the adsorbate aromatic ring, one above a hydrogen atom in the adsorbate alkyl chain, and

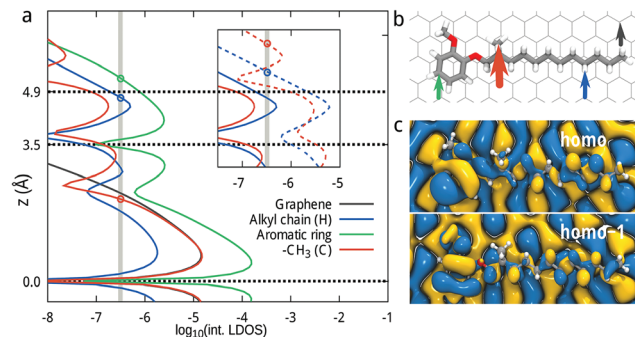


Fig. 5 Image contrast depends on the $iLDOS$ decay in space. (a) Image height (z , in Å) as a function of $\log(iLDOS)$ for points set at the graphene, the aromatic fragment of cMPE-OC₁₂(S), an alkyl chain hydrogen atom, and the methyl marker carbon atom at small ($i = 4$) and large ($i = 14$, dashed lines in the inset) bias voltage. The grey vertical line represents a typical constant current value in experimental STM imaging. (b) Atomic model of cMPE-OC₁₂(S) adsorbed on graphene, with the four analysis points marked with color-coded arrows. (c) HOMO and HOMO–1 of the system at an isovalue of 0.0001, as per 100PBE calculations.

one above the carbon atom in the methyl marker. In Fig. 5(b) these four points are marked with color-coded arrows. The vertical axis of the plot represents the direction in which the (Tersoff–Hamann) tip approaches the adsorbate–substrate system, and the horizontal axis is proportional to the logarithm of the imaging isocurrent. The top four occupied orbitals were included in the low bias voltage $iLDOS$ curves. Large bias voltage curves, represented by dashed lines in the inset plot, correspond to the top 14 occupied orbitals. At very large distances above the system, the atom-centered Gaussian basis set used in the 100PBE calculations decays too rapidly, so the exponential tail of the electron density is poorly or not at all described. However, the relevant region for the images, as shown in Fig. 5, is relatively close to the alkyl chains, and the basis set used here is still more than able to describe electron density.

As estimated previously, the range of $iLDOS$ values comparable to experiment is approximately 10^{-6} to 10^{-7} . Hence, we center our analysis of the plot on values of the $iLDOS$ close to 5×10^{-7} e bohr⁻³, marked with a grey vertical line in Fig. 5a. Image heights, that is, the highest z points at which the required value of the $iLDOS$ is met, are marked with circles. The sharp horizontal wells correspond to atomic nuclei, where there is no electron density in the relevant energy regime. The behavior of the curves in the bottom half of the plot ($z < 2.5$ Å) is due to electron density associated with the graphene substrate, whose nuclei lie at 0.0 Å (marked by a dotted horizontal line). Since the four points compared are situated in non-equivalent places above the graphene, the magnitudes of the curves in this region of the plot are not all the same.

The top half of Fig. 5 ($z > 2.5$ Å) corresponds to the adsorbate region, whose carbon nuclei lie close to 3.5 Å when in the aromatic ring, 3.6 Å when in the alkyl chain, and 4.9 Å when in the methyl carbon atom (signaled by a dotted horizontal line). At low bias voltage (continuous lines), the brightest section of the image corresponds to the aromatic ring at an

apparent height of 5.3 Å and *not* to the methyl marker. Moreover, in order to reach the imposed isocurrent value, according to these calculations, the Tersoff–Hamann tip needs to approach as close as 2.1 Å from the graphene. That corresponds to a position *below* the nuclei of cMPE-OC₁₂(S) – a prediction which as already noted above is a problematic feature of the perturbative approach embodied by the Tersoff–Hamann approximation. Even the alkyl chain hydrogen appears at higher *z*, 4.8 Å. Examining the top occupied molecular orbitals of the system, a lack of amplitude in the methyl group is observed again. As an example, the HOMO and HOMO-1 as shown in Fig. 5c. At large bias voltage, on the other hand, the local charge density is higher and more electronic states may contribute to the tunneling. Hence, the local charge density in the marker ‘overtakes’ that of the alkyl chain hydrogen and thus appears brighter by approximately 0.7 Å.

While the distances in this plot cannot be taken as a quantitative measurement, it seems clear that an abrupt and important decrease in the charge density (hence tunneling probability and tip height) takes place when the tip approaches the methyl marker at low bias voltage. Furthermore, the change in relative position of the curves with the bias voltage provides, to a certain extent, clarification to the bias-dependent marker contrast reversal. A more realistic picture would need to consider the whole substrate, the bulk of the tip and the dynamics of the system within a more accurate approach that goes beyond the perturbative Tersoff–Hamann approach.

3.3.3 Calculated images of tDBA-OC₇: marker orientation. We then consider our third and largest model, which contains the whole DBA aromatic core with its three aromatic rings (tDBA-OC₇, Scheme 1). As indicated previously, this model is composed by a truncated DBA structure with interdigitated alkyl chains on top of a graphene substrate. In terms of electronic structure, the main difference with respect to the other models studied here is the considerable size of the aromatic core, which shifts the molecular HOMO still higher in energy. According to our PBE periodic calculations for the adsorbate–substrate system, the highest energy state localized in the molecule is less than 0.2 eV below the Fermi level of the graphene, significantly closer than for octane, MPE-OC₁₂, and their derivatives (Fig. S2†).

We calculated images of the reference model (in which the tDBA-OC₇ molecule is unmodified) and its methylated derivatives in the ‘up’ and ‘down’ orientation at a series of increasing bias voltages. This was done by gradually increasing the number of occupied orbitals included in the integration of the local density of states, as explained before. In this case, the images calculated by integrating the 4 and 8 top occupied molecular orbitals provide representative examples of the small and large bias voltage regimes. Fig. 6 summarizes the results in a comparison between the simulated images at small and large bias voltage of the reference DBA model (tDBA-OC₇) and its methylated derivative in the ‘up’ and ‘down’ orientation. The hydroxylated derivative images, also included in the figure for the sake of conciseness, are discussed in section 3.4. We chose to display only two complete

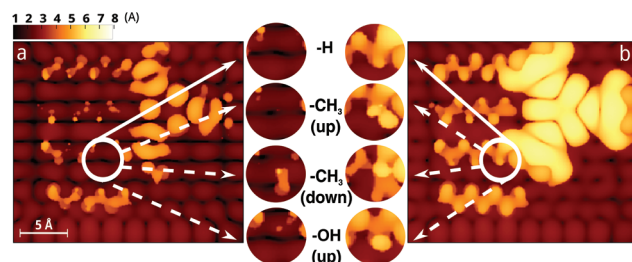


Fig. 6 STM simulated images of tDBA-OC₇ derivatives. (a) Small bias voltage (*i* = 4) image of tDBA-OC₇, with zoomed cutouts corresponding to the chiral marker area (encircled in white in the main image) in the tDBA-OC₇ image and the analogous tcDBA-OC₇(up), tcDBA-OC₇(down) and tcDBA-OC₇(OH-up) images; and (b) its large bias voltage (*i* = 8) equivalent. The value of the integrated LDOS is 10^{-6} e bohr⁻³, and the scale is in Å.

images, those of the unmodified tDBA-OC₇ at small (Fig. 6a) and large (Fig. 6b) bias voltage, as the calculated images in the regions with identical molecular structure appear almost identical for all tDBA-OC₇ derivatives. The areas enclosed by a white circle correspond to the regions where one of the markers is located in the chiral derivatives. The other marker (attached to C2 of the other DBA alkyl chain) is situated too close to the graphene flake edge, and hence we did not consider its LDOS representative of the environment of the markers in a DBA film. The array of magnified cutouts between the main images is meant to facilitate the comparison between the reference model and its marked derivatives. These cutouts belong to the chiral marker region from equivalent (*i.e.* same bias voltage and isocurrent) simulated images of the aforementioned tDBA-OC₇ derivatives. It is to be noted that all calculated images in Fig. 6 are based on 100PBE; periodic SIESTA calculations with PBE lead to such extensive density leakage from the aromatic core the whole chiral marker region (including the terminal parts of the interdigitated chains) is completely swamped at all bias voltages.

The main features of the calculated images in the areas outside the marker region correspond to the aromatic core and the alkyl chains. The large DBA-like aromatic core appears as a bright triangular shape that reflects its threefold symmetry. The alkyl chain features can be identified, as in the previous cases, by bright zig-zag patterns. On the other hand, contrast in the marker region varies depending on the ‘up’ or ‘down’ orientation of the marker. The small bias voltage images of the ‘up’ methylated compound are largely identical to those of the unmodified compound, despite the different chemical nature of the bulky methyl group that substitutes the hydrogen atom in the stereogenic carbon. In some of them, like the one shown in Fig. 6 (-CH₃ (up) cutout), the height in the marker position is that of the graphene, even if alkyl chain features are clearly identifiable in the rest of the system. This could be indeed the ‘dark spot’ that appeared in the previous models (4-methyloctane and cMPE-OC₁₂(S)) persisting despite the enlargement of the aromatic core. Whether this lack of bright features in the methyl marker region at low bias voltage

can explain the ‘dark contours’ that appear on chiral DBA molecules in experimental images will be discussed in section 3.5. In the large bias voltage images the marker can be immediately recognized as a bright feature.

Small bias voltage images suggest that when the methyl group in tcDBA-OC₇ is pointing down, towards the surface, no ‘dark spot’ is observed. An increase in the bias voltage leads to a brighter spot which corresponds to the hydrogen atom, and a darker feature at lower height which corresponds to the methyl marker. Interestingly, the features of the alkyl chain where the marker is located appear noticeably darker than the interdigitated alkyl chains and the equivalent alkyl chain in the reference compound. This happens in both small and large bias voltage images. The cause is that the presence of the marker pushes slightly the alkyl chain further away from the surface. The electronic coupling of the alkyl chain with the graphene diminishes and so does the local density of states in the required energy range, hence the darker features.

Overall, the shape of the features in the calculated images is in good agreement with experimental observations. The relative height of the LDOS in the aromatic core with respect to the LDOS in the alkyl chains ranges from 1 to 3 Å, depending on the bias voltage. Experimentally, this relative height may vary between 2 to 4 Å at bias voltage values of -0.2 V and iso-currents close to 0.2 nA. A typical experimental image line profile of a mixture of chiral and achiral molecules is shown in Fig. 7a. These values are in reasonably good agreement. The underestimation in the simulated images may stem from a slightly overcontracted charge density in the aromatic core due to the 100% HF exchange used to calculate them. The experimental STM studies reported on chiral DBA molecules focus on the images at bias voltages in which the ‘dark contours’ can be clearly identified. However, these computational results prompted a search through discarded images at larger bias voltages. The lack of ‘dark contours’ in these images and even the seemingly enlarged bright chiral DBA core features are in good agreement with the computational prediction (Fig. 7b).

3.4 Simulated images of hydroxylated molecules

So far, we have discussed in detail how the calculated STM images of the reference systems in this study change when a methyl marker is added to the octane, MPE-OC₁₂ or tDBA-OC₇ molecules. The following section will address the effect of adding hydroxy markers instead. We will pay particular attention to the differentiating elements between images of the hydroxylated and the methylated systems.

3.4.1 Calculated images of octan-4-ol. Calculated images of octan-4-ol on graphene, the simplest hydroxylated model considered in this study, illustrate the contrast variation in the marker region. As before, we calculated a series of images at increasing values of the bias voltage (see S6.4†). Then we selected two images as the most representative of the small ($V_{\text{bias}} = -0.6$ V) and large ($V_{\text{bias}} = -2.0$ V) bias voltage regimes. These images are displayed in Fig. 8(a and b). They were calculated using the PBE functional together with a periodic graphene substrate, as in Fig. 2. An extra image calculated with

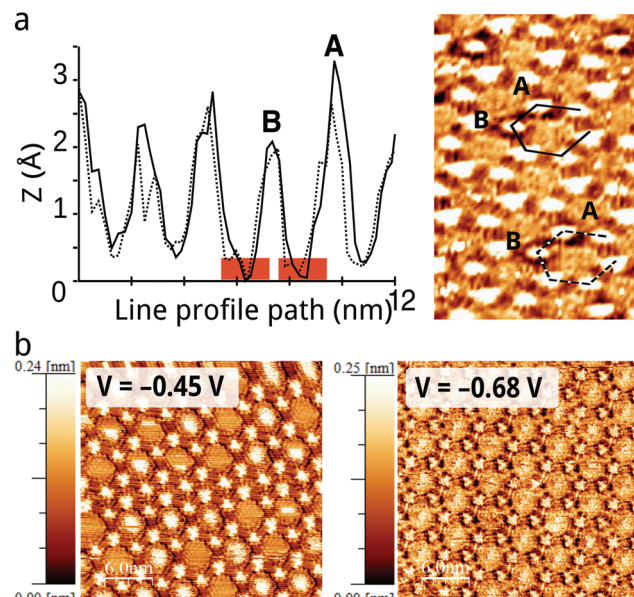


Fig. 7 Experimental STM images of chiral DBA derivatives. (a) Two line profiles (solid and dashed lines) and STM image of a mixture of cDBA-OC12(R)-OC13(S) and DBA-OC12 on HOPG ($V_{\text{bias}} = -0.2$ V, $I_{\text{set}} = 0.21$ nA). The red rectangles mark the wells corresponding to the ‘dark contours’. The chiral molecules in each line profile are labelled as A and B. (b) STM images of cDBA-OC13(R) on HOPG at $V_{\text{bias}} = -0.45$ V ($I_{\text{set}} = 0.18$ nA), in which all the molecules have ‘dark contours’, and at $V_{\text{bias}} = -0.68$ V ($I_{\text{set}} = 0.13$ nA), in which the ‘dark contours’ are no longer visible. The size-scale spans 6.0 nm.

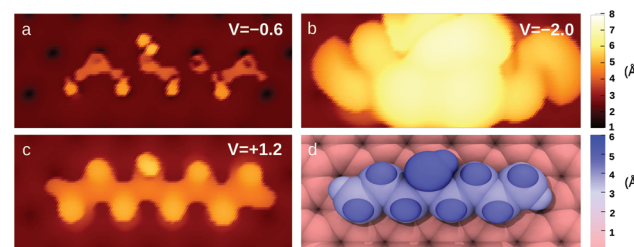


Fig. 8 Constant-current simulated images of octan-4-ol on graphene at bias voltage $V_{\text{bias}} = -0.6$ V (a), $V_{\text{bias}} = -2.0$ V (b), and $V_{\text{bias}} = +1.2$ V (c) using PBE and an integrated LDOS value of 10^{-6} e bohr⁻³; geometry of octan-4-ol on graphene coloured according to the z-coordinate of atom nuclei (d). The colour scales indicate height in angstroms.

positive bias voltage (Fig. 8c) is included in order to compare with experiment, as well as a van der Waals sphere model of the geometry used in these calculations.

The first noticeable feature of the small bias voltage image of octan-4-ol (Fig. 8a) is the lack of ‘dark spot’. A small lobular feature, slightly brighter than the surrounding methylene features, indicates the presence of the hydroxy marker. The marker region is, on the other hand, noticeably brighter than the surrounding area in the large bias voltage images. These observations are in good agreement with the results reported in ref. 19, which involve experimental STM images of films formed by long alkanes with secondary hydroxy groups de-

posited on HOPG surfaces. In that study, bright spots associated with the -OH functional groups could be imaged at bias voltages between -1.2 and -1.5 V. However, at smaller values of the bias voltage, the markers could not be identified in the images. Quantitative experimental reports such as ref. 37 estimate the relative height of the bright spot region with respect to the methylene features to be 0.30 ± 0.05 Å ($V_{\text{bias}} = +1.210$ V, $I_{\text{set}} = 200$ pA). In the calculated images at $V_{\text{bias}} = +1.2$ V (such as Fig. 8c) this relative height is close to 0.3 Å, in excellent agreement.

Ultimately, these images present two main differences with respect to the ones of 4-methyloctane. The first, as mentioned above, is the lack of a 'dark spot'. The second may be better understood by looking back at Fig. 2, and comparing the images of 4-methyloctane and octan-4-ol calculated at bias voltage $V_{\text{bias}} = -2.0$ V (Fig. 2(b) and Fig. 8(b), respectively). It seems clear that the height of the integrated LDOS is much larger above the hydroxy marker region than above the methyl marker region, by almost 1 Å. The relative height may be affected by the approximations made in image calculation. However, the noticeable difference between images opens the door to STM experimental distinction between both markers in films formed by molecules with secondary methyl and hydroxy functional groups (see Discussion section).

The chemical nature of the marker region in octan-4-ol and in 4-methyloctane is quite different. The hydroxy functional group is less bulky and more electronegative than the methyl secondary group. The details of the distinct electronic structures of both systems (4-methyloctane and octan-4-ol on graphene) provide an explanation of the differences observed in the calculated images. The HOMO of octan-4-ol is mostly localized in the lone pairs of the marker oxygen atom unlike in 4-methyloctane, in which it is delocalized throughout the σ skeleton of the main alkyl chain. It is also significantly closer to the Fermi level of the system, by approximately 1.5 eV, whereas this difference is in the range of 2.8 eV for 4-methyl-octane. As a result, the HOMO coupling with the substrate is larger. The local density of states in the hydroxy marker is then sufficient to reach the value required in the imaging conditions and produce a signal. Hence the lack of 'dark spot' at small bias voltages and the greater value of the integrated LDOS height at large bias voltages. It should be noted that in this case, images calculated with the 100PBE functional and a graphene flake as substrate (see S6.4†) are not completely similar to the ones displayed in Fig. 8, as it happened for 4-methyloctane. The HOMO in these calculations is less localized in the oxygen atom. The integrated LDOS is hence smaller within the narrow energy range used in the integration, and thus the relative image height of the marker with respect to the surrounding methylenes is smaller.

Let us examine the effects of introducing a small aromatic fragment (the 2-methoxyphenyl ether functional group) near the marker in the cMPE-OC₁₂(S)-OH molecule. As in the reference molecule and in the methyl derivative, the HOMO of the molecule is localized in the aromatic fragment, closer in energy to the Fermi level of the system by 0.7 eV.

Since in the previous section we reported the log(I)– z plot for the methylated derivative of MPE-OC₁₂ (Fig. 5a) on graphene, we found interesting to do the same for the MPE-OC₁₂ hydroxylated derivative (Fig. 9). This provides the means to compare the decay in space of the charge density for the methyl marker and the hydroxy marker. The integrated LDOS data used to produce the plot was calculated, again, with 100PBE functional and a graphene flake as substrate. The reasons and implications of these restrictions (*i.e.* regarding self-interaction error or bias voltage) have been discussed in the previous section. A sample of the simulated images of cMPE-OC₁₂(S)-(OH) is provided in the ESI (S6.7†). The analysis points above the graphene, the alkyl chain hydrogen atom and the aromatic fragment are the same as in Fig. 5. The corresponding curves are very essentially identical. In the previous section we have examined carefully the shape and relative position of these curves. Therefore, we will now focus on the particularities that arise because of the presence of the hydroxy marker instead of the methyl marker, and hence on the curve corresponding to the hydroxy marker.

The hydroxy marker analysis point is set above the oxygen atom. The resulting curve is quite different to that of the methyl marker. At small bias voltage (and considering again a 5×10^{-7} e bohr⁻³ isocurrent), the integrated LDOS height above the oxygen atom is the same as above the alkyl chain hydrogen atom. In contrast, the large bias voltage curves (dashed lines in the inset) reveal a 0.33 Å difference in height between the integrated LDOS above the marker and the integrated LDOS above the alkyl chain hydrogen atom. Also, the parallel slope of the curves indicates that this height difference is maintained over a range of isocurrent values around 5×10^{-7} e bohr⁻³. This variation of the relative height between

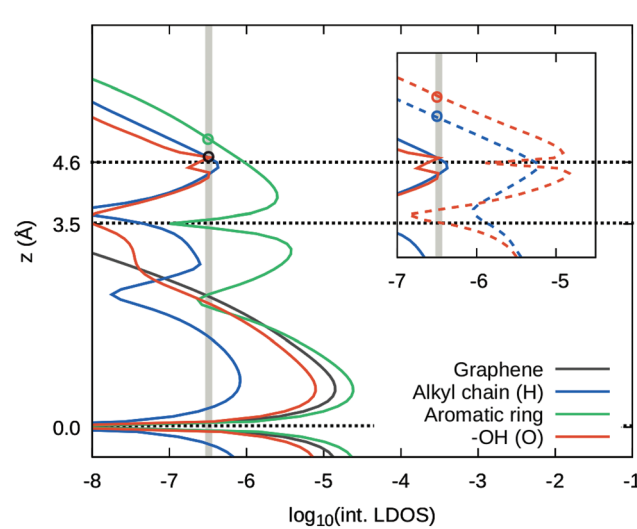


Fig. 9 Image height (z , in Å) as a function of $\log_{10}(\text{int. LDOS})$ for points set at the graphene, the aromatic fragment of cMPE-OC₁₂(S)-OH, an alkyl chain hydrogen atom, and the hydroxy marker oxygen atom at small ($i = 4$) and large ($i = 14$, dashed lines in the inset) bias voltage. The grey vertical line represents a typical constant current value in experimental STM imaging.

the marker and the methylene features with bias voltage is quite similar to the one obtained from the images of octan-4-ol calculated with 100PBE functional.

The influence of enlarging the molecular aromatic core on the marker appearance can be examined using the calculated images of the third model, tcDBA-OC₇(OH) on graphene (Fig. 6). We will focus on the appearance of the hydroxy marker region, since the remaining features of each image (*i.e.* those corresponding to the graphene, aromatic core, and alkyl chains outside the marker region) are largely identical to those of the reference compound. The key aspects of these common features have already been described in the previous section. Noticeably, there is no bright marker features whatsoever in the small bias voltage image of the region, much in the way of a ‘dark spot’. The lack of (almost any) features make its appearance quite similar to that of the reference compound. This presents a sharp contrast with the equivalent images of octan-4-ol and cMPE-OC₁₂(S)-OH, in which the features of the hydroxy markers are visible whenever the rest of the alkyl chain is (S6.4†). On the other hand, the large bias voltage image of the marker region is in very good agreement with the results for the other two hydroxylated molecules and appears quite bright.

One may wonder why the small bias voltage integrated LDOS above the marker is so different in cMPE-OC₁₂(S)-OH and tcDBA-OC₇(meso)-OH. A closer look at Fig. 9 suggests an answer: it is just a small variation in the integrated LDOS value that has a dramatic effect in the calculated images. The curve that corresponds to the marker in Fig. 9 decreases slightly below the alkyl chain hydrogen at values of the integrated LDOS below 3×10^{-7} e bohr⁻³. This would mean that a calculated image of cMPE-OC₁₂(S)-OH using said parameters (small bias voltage and 3×10^{-7} e bohr⁻³) would also have no sign of marker features. These ‘dark spots’ indicate an abrupt decrease of the LDOS in the region with respect to the surroundings. Hence, it would be interesting to compare, as we have done before for 4-methyloctane, what is the relationship between the LDOS isosurface and the vdW surface of the system in the marker region as compared to the rest of the molecule.

To establish a proper analogy, we will consider now the distances between the vdW surface and the integrated LDOS isosurface in three specific points of the calculated images: above the marker oxygen atom in tcDBA-OC₇(OH), above the topmost hydrogen atom in the methyl marker of tcDBA-OC₇, and above a hydrogen atom further in the alkyl chain of tcDBA-OC₇(OH), which we will use as reference.

The van der Waals surface above the marker oxygen atom lies at $z = 6.41$ Å,§ while the integrated LDOS height at small and large bias voltage lies at $z = 2.0$ Å and 5.5 Å, respectively. The difference implies that the integrated LDOS isosurface is 4.4 and 0.9 Å below the vdW surface, respectively. Proceeding in a similar way, those distances become 4.5 Å and 1.0 Å above

the methyl marker of the methylated DBA derivative. For the reference hydrogen atom in the alkyl chain, on the other hand, the LDOS isosurface passes below the vdW surface by 1.1 and 0.5 Å, following a similar line of reason as before. The differences, specially at low bias, are quite striking. Although these numbers are not to be taken quantitatively due to the shortcomings and approximations of the computational method, they indicate, as mentioned before, a clear disruption in the integrated LDOS. Whether the experimental tip would actually cross so starkly the van der Waals surface of the film in the marker region will be discussed in the following section.

3.5 General discussion

The discussion in the Results section raises a number of general questions which we wish to revisit here. The first concerns the role of the DFT self-interaction error in the calculation of STM images. The SIE has been known for a long time, and various methodologies are available for performing SIE-free calculations, or at least calculations in which this effect is minimized. In the context of STM image computation, GW theory and DFT+U approaches have been applied for this purpose.^{38,39} In one of these studies, the effect of correcting for the SIE on calculated images was explicitly addressed, and found to be important.¹⁸ The present case of methyl chiral markers appears to be an extreme manifestation of the distortions created in STM images by the SIE. The proximity of the markers to the high-energy states in the DBA core makes the calculated images very sensitive to the LDOS decay in both the vertical and in-plane directions. This is particularly true because the signature of the markers in the experimental images is only apparent for a small range of bias voltage and isocurrent values, so that relatively small errors in the calculated LDOS can make it impossible to reproduce or account for experimental features. Monolayers of organic adsorbates with relatively electron-rich and electron-poor regions present quite stark variations in LDOS values so the presently observed anomalies with GGA functionals may be quite widespread. To our knowledge, there has been no previous discussion of the role of SIE for STM image calculation for organic monolayers.

Another general aspect concerns the relation between the calculated image heights and the tip heights during experiments, both in a relative sense (difference between two locations) and in an absolute sense (actual tip height *vs.* calculated height). As discussed in several places above, the relative heights (between marker and methylene features, for instance) computed here match well those obtained in experiments.³⁷ Comparisons regarding absolute height, however, are much more complex. The height scale in the topography channels of constant-current STM images is relative to the lowest and highest point in the image and gives no indication of the absolute separation from the surface. Distances below 8 Å have been reported from measurements on hysteretic currents due to tip–substrate mechanical interactions on bare graphene surfaces.⁴⁰ For HOPG with an interfacial water layer, an experimental study on the tip–surface separation range (that is, between zero tunneling current and mechanical contact,

§ Assuming the van der Waals radius (r_{vdw}) of the oxygen atom to be 1.56 Å (as in the OPLS-AA force field) and the nuclei atom position to be $z = 4.85$ Å

defined as zero local barrier height) narrows the distance down to 1–3 Å at a bias voltage of −0.2 eV and tunneling currents below 1 nA.⁴¹ Accounting for the vdW radii of the carbon atoms, the nuclei-to-tip distance may be ~3–5 Å away from the graphene. The main difference with the systems reported here would lie in the interfacial water layer, which contributes to the tunneling current and hence increases the sample–tip separation. On the other hand, computational papers can provide also calculated values for comparison. For instance, for ESQC calculations of polycyclic aromatic hydrocarbons on graphene, including the tip explicitly, constant-current image heights range from 5 to 8 Å above the adsorbed molecules.⁴² Calculations of polythiophenes on graphene, also with an explicit tip, yield heights of the order of 8–9 Å ($V_{\text{bias}} = -1.5$ V, $I_{\text{set}} = 0.1$ nA).⁴³ The calculated heights reported here are, then, within a reasonable range.

The third question derives from the previous one. If the calculated image heights predicted here are reasonable, then what does it mean when in some regions (*i.e.* the ‘dark spots’) the integrated LDOS is significantly below the vdW surface of the imaged system? This would imply that the Tersoff–Hamann s-orbital tip and the adsorbate are in vdW contact (and even a large overlap) in those regions, and it is unphysical to model this situation as a tunneling process. As mentioned before, the lack of marker features in the ‘dark spots’ is to be taken as the warning sign of an abrupt depletion of the integrated local density of states. The reason for this is a hindered coupling with the graphene surface. The coupling between the graphene and the marker groups is reduced partly because of the larger marker-graphene separation, as compared to the rest of the molecule, and partly due to the electronic structure of the molecule itself. The high energy states that contribute to the tunnelling lack amplitude in the marker regions, specially (and remarkably) in the case of methyl markers. It seems safe to assume, also, that the tip may get very close to the adsorbed molecule in those regions. These results map relatively well into the experimentally observed ‘dark contours’. However, the situation described here is static, and STM images are acquired under dynamic conditions. Hence, other factors may contribute to the imaging of ‘dark contours’.⁴⁴ For instance, the esteric hindrance caused by the presence of the markers may cause a higher mobility of the alkyl chain, further diminishing the coupling with the substrate and hence the local density of states available for producing the necessary isocurrent.

To finish, how can we use the information provided by these calculations to improve future experiments? The differences in the marker region between methyl and hydroxy markers in images calculated with different bias voltages suggest two ideas. First, we provide a frame of orientative bias voltages at which each marker can be visualized. In a mixture of methylated and unmethylated alkanes, for instance, the marked molecules may be possible to differentiate at small bias voltages (as a speculation, between −0.2 and −0.6 V) by dark spots, much as like it happens with the DBAs. A similar reasoning can be implemented in a mixture of alkanes and secondary alcohols at large bias voltage. These kind of mix-

tures are of interest because of how the inherent chirality of the marker may affect the self-assembly process of the film. And second, we suggest a procedure for discriminating between hydroxy and methyl markers. Consecutive constant-current (or constant-height, for that matter) scans at increasing bias voltage over small surface areas may result in a ‘traffic light’ effect, in the sense that both marked molecules may present dark spots at very low bias voltages, then only the methyl marker will appear dark at a slightly larger bias voltage, and lastly both markers may appear bright at a large bias voltage (with OH predicted to be somewhat brighter than CH₃). That is, a time-dependent, *x*-*y* resolved Z–V spectra. This type of measurements could potentially open the door to chemical identification in room-temperature, liquid–solid interface STM experiments.¶

4 Conclusions

Aided by computation, we have obtained suitable geometries to represent octane, a DBA derivative and an intermediate molecule adsorbed on graphene/graphite substrates, together with their chiral derivatives containing methyl and hydroxy STM markers. Conformations where the marker is directed towards the solvent seem clearly more energetically favoured for the methylated derivatives, while hydroxylated molecules remain ambiguous. Image simulation parameters estimated from first principles allowed us to reliably calculate images of the models at a series of bias voltages, revealing methyl markers to have stark contrast variations depending on the imaging bias voltage. Low bias voltage images present dark spots in the marker regions due to a lack of local density of states in the relevant energy regime. This is partly due to sigma-hyperconjugation and lower surface-molecule electronic coupling in the marker region, which not only does not produce current signal but hampers tunneling from the molecular skeleton too. This provides insight into the ‘dark contours’ observed in DBA. From a computational perspective, self-interaction errors create unphysical effects in systems with (not so) large aromatic fragments, which were avoided using in-house code to simulate the images with Gaussian 09. According to our calculations, hydroxy markers show a similar behaviour (a void in image height) in a smaller range of bias voltages. While only one marker is needed for bi-component achiral/chiral systems, plausible differentiation between methyl and hydroxy markers using small bias voltage adjustments opens the door for the investigation of complex multi-component systems and phenomena simultaneously tracing chemically different markers.

¶We note that this procedure is intrinsically different from Scanning Tunneling Spectroscopy (STS). With STS, current–voltage spectra of specific points in the molecular layer can be acquired under restrictive conditions (*i.e.* ultra high vacuum and extremely low temperatures). Hence, it is unsuitable for room-temperature liquid–solid interface experiments in which the thermal drift prevents the localization of the tip.

Conflicts of interest

There are no conflicts to declare.

Acknowledgements

JNH and ASM would like to thank the KU Leuven for financial support.

References

- 1 S. D. S. Hazen and M. Robert, *Nat. Mater.*, 2003, **2**, 1476–1122.
- 2 H.-S. Wang and J.-P. Wei, *Nanoscale*, 2015, **7**, 11815–11832.
- 3 L. Perez-Garcia and D. B. Amabilino, *Chem. Soc. Rev.*, 2007, **36**, 941–967.
- 4 M. M. Green, N. C. Peterson, T. Sato, A. Teramoto, R. Cook and S. Lifson, *Science*, 1995, **268**, 1860–1866.
- 5 P. Iavicoli, H. Xu, L. N. Feldborg, M. Linares, M. Paradinas, S. Stafström, C. Ocal, B. Nieto-Ortega, J. Casado, J. T. López Navarrete, R. Lazzaroni, S. D. Feyter and D. B. Amabilino, *J. Am. Chem. Soc.*, 2010, **132**, 9350–9362.
- 6 G. Schull, H. Ness, L. Douillard, C. Fiorini-Debuisschert, F. Charra, F. Mathevet, D. Kreher and A.-J. Attias, *J. Phys. Chem. C*, 2008, **112**, 14058–14063.
- 7 J. R. Reimers, D. Panduwinata, J. Visser, Y. Chin, C. Tang, L. Goerigk, M. J. Ford, M. Sintic, T.-J. Sum, M. J. J. Coenen, B. L. M. Hendriksen, J. A. A. W. Elemans, N. S. Hush and M. J. Crossley, *Proc. Natl. Acad. Sci. U. S. A.*, 2015, **112**, E6101–E6110.
- 8 L. C. Giancarlo and G. W. Flynn, *Acc. Chem. Res.*, 2000, **33**, 491–501.
- 9 Y. Fang, E. Ghijssens, O. Ivasenko, H. Cao, A. Noguchi, K. S. Mali, K. Tahara, Y. Tobe and S. De Feyter, *Nat. Chem.*, 2016, **8**, 711–717.
- 10 E. Ghijssens, H. Cao, A. Noguchi, O. Ivasenko, Y. Fang, K. Tahara, Y. Tobe and S. D. Feyter, *Chem. Commun.*, 2015, **51**, 4766–4769.
- 11 K. Tahara, H. Yamaga, E. Ghijssens, K. Inukai, J. Adisoejoso, M. O. Blunt, S. De Feyter and Y. Tobe, *Nat. Chem.*, 2011, **3**, 714–719.
- 12 C. L. Claypool, F. Faglioni, A. J. Matzger, W. A. Goddard and N. S. Lewis, *J. Phys. Chem. B*, 1999, **103**, 9690–9699.
- 13 J. E. Bello, J. S. McElfresh and J. G. Millar, *Proc. Natl. Acad. Sci. U. S. A.*, 2015, **112**, 1077–1082.
- 14 S. De Feyter, A. Gesquière, P. C. M. Grim, F. C. De Schryver, S. Valiyaveettil, C. Meiners, M. Sieffert and K. Müllen, *Langmuir*, 1999, **15**, 2817–2822.
- 15 S. De Feyter, A. Gesquière, M. M. Abdel-Mottaleb, P. C. M. Grim, F. C. De Schryver, C. Meiners, M. Sieffert, S. Valiyaveettil and K. Müllen, *Acc. Chem. Res.*, 2000, **33**, 520–531.
- 16 E. Niemi and J. Nieminen, *Chem. Phys. Lett.*, 2004, **397**, 200–204.
- 17 M.-L. Bocquet and P. Sautet, *Surf. Sci.*, 1996, **360**, 128–136.
- 18 G.-M. Rignanese, X. Blase and S. G. Louie, *Phys. Rev. Lett.*, 2001, **86**, 2110–2113.
- 19 C. Le Poulenec, J. Cousty, Z. X. Xie and C. Mioskowski, *Surf. Sci.*, 2000, **448**, 93–100.
- 20 J. W. Ponder and F. M. Richards, *J. Comput. Chem.*, 1987, **8**, 1016–1024.
- 21 W. L. Jorgensen, J. P. Ulmschneider and J. Tirado-Rives, *J. Phys. Chem. B*, 2004, **108**, 16264–16270.
- 22 J. M. Soler, E. Artacho, J. D. Gale, A. García, J. Junquera, P. Ordejón and D. Sánchez-Portal, *J. Phys.: Condens. Matter*, 2002, **14**, 2745.
- 23 J. P. Perdew, K. Burke and M. Ernzerhof, *Phys. Rev. Lett.*, 1996, **77**, 3865–3868.
- 24 N. Troullier and J. L. Martins, *Phys. Rev. B: Condens. Matter Mater. Phys.*, 1991, **43**, 1993–2006.
- 25 M. J. Frisch, G. W. Trucks, H. B. Schlegel, G. E. Scuseria, M. A. Robb, J. R. Cheeseman, G. Scalmani, V. Barone, B. Mennucci, G. A. Petersson, H. Nakatsuji, M. Caricato, X. Li, H. P. Hratchian, A. F. Izmaylov, J. Bloino, G. Zheng, J. L. Sonnenberg, M. Hada, M. Ehara, K. Toyota, R. Fukuda, J. Hasegawa, M. Ishida, T. Nakajima, Y. Honda, O. Kitao, H. Nakai, T. Vreven, J. A. Montgomery Jr., J. E. Peralta, F. Ogliaro, M. Bearpark, J. J. Heyd, E. Brothers, K. N. Kudin, V. N. Staroverov, R. Kobayashi, J. Normand, K. Raghavachari, A. Rendell, J. C. Burant, S. S. Iyengar, J. Tomasi, M. Cossi, N. Rega, J. M. Millam, M. Klene, J. E. Knox, J. B. Cross, V. Bakken, C. Adamo, J. Jaramillo, R. Gomperts, R. E. Stratmann, O. Yazyev, A. J. Austin, R. Cammi, C. Pomelli, J. W. Ochterski, R. L. Martin, K. Morokuma, V. G. Zakrzewski, G. A. Voth, P. Salvador, J. J. Dannenberg, S. Dapprich, A. D. Daniels, Ö. Farkas, J. B. Foresman, J. V. Ortiz, J. Cioslowski and D. J. Fox, *Gaussian 09 Revision D.01*, Gaussian Inc., Wallingford CT, 2009.
- 26 J. Tersoff and D. R. Hamann, *Phys. Rev. Lett.*, 1983, **50**, 1998–2001.
- 27 J. Radilla, M. Galván, Y. Trinidad-Reyes and N. Batina, *MRS Online Proc. Libr. Arch.*, 2004, **838**, 010.1.
- 28 M. Willenbockel, D. Luftner, B. Stadtmüller, G. Koller, C. Kumpf, S. Soubatch, P. Puschnig, M. G. Ramsey and F. S. Tautz, *Phys. Chem. Chem. Phys.*, 2015, **17**, 1530–1548.
- 29 J. Repp, G. Meyer, S. M. Stojković, A. Gourdon and C. Joachim, *Phys. Rev. Lett.*, 2005, **94**, 026803.
- 30 W. N. Hansen and G. J. Hansen, *Surf. Sci.*, 2001, **481**, 172–184.
- 31 T. Tamura, R. Kobayashi, S. Ogata and A. M. Ito, *Modell. Simul. Mater. Sci. Eng.*, 2014, **22**, 015002.
- 32 T. Yang, S. Berber, J.-F. Liu, G. P. Miller and D. Tománek, *J. Chem. Phys.*, 2008, **128**, 124709.
- 33 B. Ilan, G. M. Florio, M. S. Hybertsen, B. J. Berne and G. W. Flynn, *Nano Lett.*, 2008, **8**, 3160–3165.
- 34 A. Minoia, I. Destoop, E. Ghijssens, S. D. Feyter, K. Tahara, Y. Tobe and R. Lazzaroni, *RSC Adv.*, 2014, **5**, 6642–6646.
- 35 J. I.-C. Wu, C. Wang, W. C. McKee, P. v. R. Schleyer, W. Wu and Y. Mo, *J. Mol. Model.*, 2014, **20**, 1–9.

- 36 T. Schmidt, E. Kraisler, L. Kronik and S. Kummel, *Phys. Chem. Chem. Phys.*, 2014, **16**, 14357–14367.
- 37 C. L. Claypool, F. Faglioni, W. A. Goddard, H. B. Gray, N. S. Lewis and R. A. Marcus, *J. Phys. Chem. B*, 1997, **101**, 5978–5995.
- 38 K. H. Bevan, F. Zahid, D. Kienle and H. Guo, *Phys. Rev. B: Condens. Matter Mater. Phys.*, 2007, **76**, 045325.
- 39 N. A. Wasio, R. C. Quardokus, R. P. Forrest, S. A. Corcelli, Y. Lu, C. S. Lent, F. Justaud, C. Lapinte and S. A. Kandel, *J. Phys. Chem. C*, 2012, **116**, 25486–25492.
- 40 M. Yankowitz, K. Watanabe, T. Taniguchi, P. San-Jose and B. J. LeRoy, *Nat. Commun.*, 2016, **7**, 13168.
- 41 J. Hahn, Y. Hong and H. Kang, *Appl. Phys. A*, 1998, **66**, 467–472.
- 42 Y. J. Dapke, M. Andersen, R. Balog, L. Hornekær and X. Bouju, *Phys. Rev. B: Condens. Matter Mater. Phys.*, 2015, **91**, 045427.
- 43 A. Rochefort, S. Bedwani and A. Lopez-Bezanilla, *J. Phys. Chem. C*, 2011, **115**, 18625–18633.
- 44 R. L. Hayes and M. E. Tuckerman, *J. Phys. Chem. C*, 2010, **114**, 15102–15108.